Hydraulic fracture energy budget: Insights from the laboratory

S. D. Goodfellow[1,2], M. H. B. Nasseri[1], S. C. Maxwell[2], and R. P. Young[1]

[1] Department of Civil Engineering, University of Toronto, Toronto, Ontario, Canada, [2] IMaGE, Itasca Calgary, Calgary, Alberta, Canada

Abstract In this paper we present results from a series of laboratory hydraulic fracture experiments designed to investigate various components of the energy budget. The experiments involved a cylindrical sample of Westerly granite being deformed under various triaxial stress states and fractured with distilled water, which was injected at a range of constant rates. Acoustic emission sensors were absolutely calibrated, and the radiated seismic energy was estimated. The seismic energy was found to range from 7.02E−8% to 1.24E−4% of the injection energy which is consistent with a range of values for induced seismicity from field-scale hydraulic fracture operations. The deformation energy (crack opening) of the sample during hydraulic fracture propagation was measured using displacement sensors and ranged from 18% to 94% of the injection energy. Our results support the conclusion that aseismic deformation is a significant term in the hydraulic fracture energy budget.

1. Introduction

Microseismic imaging technology is used to visualize the evolution of hydraulic fracture geometry, which allows engineers to optimize the recovery of hydrocarbons from unconventional reservoirs. Microseismic events are analyzed for location, magnitude, dimension, and mechanism, which are then used to estimate the extent of seismic deformation; however, the principal deformation mechanisms responsible for stimulation are still poorly understood. It is well documented that during hydraulic fracture treatments in the field, the amount of energy radiated as seismic waves is a very small component of the total input energy (injection energy), which suggests that seismic energy production is a relatively inefficient process. In observations across a range of unconventional hydraulic fracture stimulations, the radiated seismic energy is ≪ 1% of the injection energy [*Maxwell et al.*, 2008; *Boroumand and Eaton*, 2012; *Warpinski et al.*, 2012].

Warpinski et al. [2012] presented an example to highlight the contrast between injection energy and seismic energy. A conservative estimate of 1000 − 2.0 M_w microseismic events produced during one hydraulic fracture treatment stage would amount to 63 kJ, whereas the injection energy for a typical fracture stage would be 135 GJ. The work done to open a hydraulic fracture of common dimensions 600 m wing length, 90 m height, and 5 mm opening, pumped at 50 MPa corresponds to 27 GJ, which is roughly 20% of the injection energy. Fracture geometry is determined via interpretation of the microseismic cloud, and therefore, the opening energy could be misrepresented. In the field, the deformation energy is estimated to range from 15% to 80% of the injection energy [*Maxwell et al.*, 2008; *Boroumand and Eaton*, 2012; *Warpinski et al.*, 2012]. When considering that the injection energy is on the order of a million times greater than the seismic energy, it is reasonable to conclude that the propagation of a hydraulic fracture is a largely aseismic process and analysis of injection pressure and downhole tiltmeter data confirms this [*Maxwell*, 2011; *Warpinski et al.*, 2012]. Downhole tiltmeter data reflect the opening behavior of a hydraulic fracture, and the tiltmeter spectrum shows that the majority of deformation is occurring at frequencies orders of magnitude lower than the seismic range [*Warpinski et al.*, 2012].

To study the energy budget in more detail and control variables that are unknown in the field, a series of laboratory hydraulic fracture experiments were conducted, where fluid pressure, seismicity, fracture opening, and fracture surface area were monitored with calibrated instruments allowing for quantification of these energy budget components.
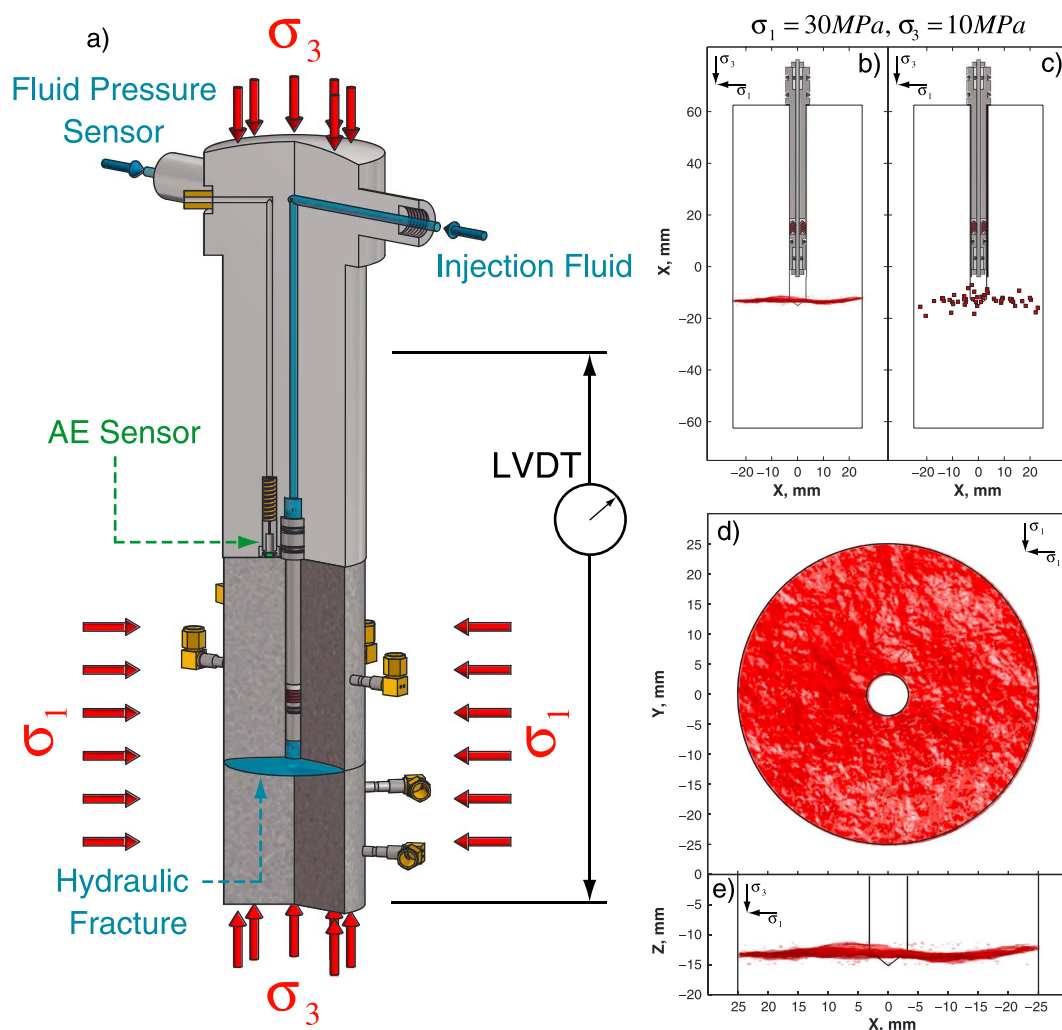
Figure 1. (a) Laboratory hydraulic fracture apparatus. Experiment SR4 (σ_1 = 30 MPa, σ_3 = 10 MPa), (b, e) μCT fracture surface projected on the $\sigma_1 - \sigma_3$ plane, (c) AE event location projected on the $\sigma_1 - \sigma_3$ plane, and (d) μCT fracture surface projected on the $\sigma_1 - \sigma_1$ plane.

2. Experimental Setup, Methods, and Theory

2.1. Experimental Setup

Westerly granite was chosen because it has been studied in numerous experiments and is well suited to acoustic emission (AE) studies [*Lockner et al.*, 1991; *Thompson et al.*, 2006, 2009] because of its homogeneous and isotropic structure (mean grain size is 0.75 mm). Eight cylindrical samples 125 mm in length and 50 mm in diameter were prepared with the end faces ground and polished to within 0.01 mm parallelism using a diamond grinding wheel. Once the specimens were machined to the correct dimensions, a 6.35 mm diameter, 75 mm deep borehole was drilled along the cylinder axes (Figure 1a) using a carbide tipped masonry drill bit.

Experiments were conducted in a triaxial geophysical imaging cell (Figure 1a) where both the axial and confining pressures were maintained under load control. Axial deformation was measured using two linear variable differential transformers (LVDT) located close to the rock sample and diametral deformation was measured using a cantilever system. A unique borehole packer system was used to seal a small section at the bottom of the borehole to a maximum pressure of 70 MPa.

Acoustic Emission (AE) was monitored by 19 piezoelectric sensors (ErgoTech Ltd). AE signals recorded on 12 rubber jacket-mounted sensors were amplified by 50 dB using Applied Seismology Consultants (ASC) amplifiers with built-in 100 kHz to 1 MHz band-pass filter, and AE signals recorded on seven platen-mounted

sensors were amplified by 60 dB using Cooknell CA-6 charge amplifiers with a built-in 10 kHz high-pass filter. The ErgoTech AE sensors were absolutely calibrated in the laboratory following the methods of *McLaskey and Glaser* [2012]. The sensors were calibrated over a range of incident angles (0°–90°) and showed broadband velocity sensitivity, with no significant azimuthal dependency, between 10 kHz and 2 MHz. Amplified waveforms were continuously recorded using the ASC Richter acquisition system, which has a 10 V dynamic range. Analogue data was sampled at 10 MHz and digitized at 12 bit resolution. Ultrasonic velocities (*P* and *S* waves) were measured periodically along multiple raypaths.

Samples were initially loaded to a stress state of triaxial tension, where σ_1 was applied as the confining pressure and σ_3 was applied along the cylinder axis (Figure 1). Once the desired stress state was archived, the system was left to stabilize before fluid was injected. After approximately 15 min had elapsed, fluid was injected into the sealed section of the borehole at a constant injection rate. Fluid pressure was measured by a pressure sensor located at the injection point of the loading platen (Figure 1a). Pumping stopped after the sample failed, and the fluid pressure dropped back to σ_3.

2.2. Energy Budget

The energy balance formulation for the propagation of a hydraulic fracture in the laboratory can be expressed using the following equation:

$$E_I + \Delta W = \underbrace{E_f + E_G + E_R}_{\text{AEs}} + \underbrace{E_G + E_d + I}_{\text{HF}} \qquad (1)$$

where E_I is the injection energy supplied by the pump and ΔW is the change in elastic energy. The output side of the energy balance equation is separated into AE and hydraulic fracture (HF) components. The change in elastic potential energy (ΔW) is equal to the sum of the frictional energy dissipated on microshear planes (E_f), the fracture energy from the process zone and new surface generation of microshear failures ($E_{G_{AE}}$), and the energy radiated as ultrasonic waves (E_R) from all AE events. In this formulation, we assume that all AE events result from microshear failures, which constitutes self-consistency when using the empirical earthquake relationship of *Kanamori* [1978] and apparent stress relationship of *Wyss and Brune* [1968]. The change in elastic potential energy (ΔW) can be calculated from the following equation [*Kanamori and Brodsky*, 2004]:

$$\Delta W = \bar{\sigma} \sum_{i=1}^{n\text{AE}} Ad = \bar{\sigma} \sum_{i=1}^{n\text{AE}} \frac{M_0}{\mu} \qquad (2)$$

where $\bar{\sigma}$ is the average stress during fracturing, nAE is the number of AE events, A is the area of a microfracture event, d is the slip distance, M_0 is the seismic moment, and μ is the shear modulus (27 GPa).

For the hydraulic fracture component, $E_{G_{HF}}$ is the energy needed to create two new fracture surfaces due to hydraulic forcing, E_d is the deformation energy corresponding to the fracture opening (dilation), and I accounts for all other forms of energy loss. In this formulation, the loss term (I) accounts for viscous dissipation and fluid leak-off which are a function of rock permeability, fluid viscosity, and injection rate.

The input power of the system (hydraulic power) is the product of the injection fluid pressure (P) and the injection rate (Q). The injection rate for these experiments ranged from 0.25 to 4 mL/min and the injection pressure was measured using a pressure sensor and sampled at 5 Hz. The injection energy (E_I) was calculated by integrating the hydraulic power over the injection interval ($t_1 - t_2$) as shown in equation (3).

$$E_I = \int_{t_1}^{t_2} PQ\mathrm{d}t \qquad (3)$$

The total deformation energy corresponding to the opening of a newly formed circular crack was calculated using the following equation:

$$E_d = A \int_0^h P\mathrm{d}h \qquad (4)$$

where A is the fracture surface area and h is the opening height of the fracture, which was measured using the average from two LVDTs. During hydraulic fracture propagation, there was no change in the diametral strain, and therefore, all volume change was in the axial direction. A postmortem analysis was conducted for one experiment whereby the failed rock specimen was scanned using high-intensity X-rays and its volume reconstructed using computed tomography (Voxel = 27.9μm). MATLAB ©image segmentation and edge detection algorithms were used to identify the fracture surface and compute its area.

2.3. Seismic Energy

Traditionally, seismic energy is a difficult parameter to estimate because of issues related to high-frequency attenuation, limited frequency band [*Ide and Beroza*, 2001] and limited knowledge of the radiation pattern. Therefore, *Maxwell et al.* [2008], *Boroumand and Eaton* [2012], and *Warpinski et al.* [2012] computed seismic energy for microseism produced during hydraulic fracture treatments using an empirical relationship between seismic moment and energy [*Kanamori*, 1978]:

$$\log_{10}(E_R) = 1.5M_w + 4.8 \tag{5}$$

where M_0 is the seismic moment and E_R is the seismic energy. This relationship was calibrated for large earthquakes with apparent stress (σ_a) ranging from 1 to 5 MPa [*Kanamori and Anderson*, 1975] and assumed double-couple mechanism. However, small mining-induced seismic events have shown σ_a between 0.01 and 1 MPa [*Collins and Young*, 2000; *Kwiatek et al.*, 2011] and in situ AE events showed σ_a between 0.01 and 0.1 MPa [*Goodfellow and Young*, 2014]. We hypothesized that the *Kanamori* [1978] relationship will provide an upper bound for the radiated energy of tiny laboratory AE events, and therefore, we also calculated the seismic energy using the apparent stress (σ_a) relationship of *Wyss and Brune* [1968] assuming constant σ_a values of 0.01 MPa and 0.1 MPa.

To calculate the seismic moment, continuous AE waveforms were harvested for discrete events. P wave arrivals were manually picked, and event hypocenter locations were calculated using the downhill simplex method and a transverse isotropic velocity model. Using manually picked P wave arrival times and theoretical S wave arrival times, calculated from the measure S wave velocity structure, the individual wave phases were windowed and the velocity spectrum of each phase was calculated using the fast Fourier transform algorithm. Next, the instrument response function was deconvolved by spectral division, and the spectra were integrated to obtain the displacement spectra.

The displacement spectrum of each waveform is defined by the low-frequency spectral plateau (Ω_{0c}) and the corner frequency (f_{0c}) [*Brune*, 1970, 1971; *Aki and Richards*, 1980]. The low-frequency spectral plateau is related to the corner frequency by the relationship below:

$$\Omega(f) = \frac{\Omega_{0c}e^{\left(-\frac{\pi f R}{V_c Q_c}\right)}}{1 + (f/f_{0c})^2} \tag{6}$$

where Q_c is the frequency-independent quality factor, which represents intrinsic attenuation effects. The parameters Ω_{0c}, f_{0c}, and Q_c were fitted to the displacement spectrum using a nonlinear least squares method in the frequency range 50 kHz to 1.2 MHz. Next, the seismic moment was calculated using equation (7),

$$M_{0c} = \frac{4\pi\rho V_c^3 R\Omega_{0c}}{F_c} \tag{7}$$

where ρ is the material density, F_c is the average P or S wave radiation coefficients for a shear source ($F_\alpha = 0.52$ and $F_\beta = 0.63$) [*Boore and Boatwright*, 1984], R is the source-receiver distance, and V_c is the body wave velocity where c refers to P or S wave phase. M_0 for each event was calculated by an average weighted by the quality of the fit for S wave spectra.

3. Results

Results from eight experiments are presented in Table 1 where four experiments were conducted at a triaxial stress state where $\sigma_1 = 20$ MPa and $\sigma_3 = 10$ MPa, and the injection rate equal to 0.25, 0.5, 2, and 4 mL/min, and four experiments conducted at a triaxial stress states where $\sigma_3 = 10$ MPa and $\sigma_1 = 12, 15, 20$, and 30 MPa and the injection rate equal to 1 mL/min.

Table 1. General Results From Eight Triaxial Hydraulic Fracture Experiments[a]

Experiment	Injection Rate (mL/min)	Stress State σ_1, σ_3 (MPa)	E_I (J)	E_d (J)	E_d/E_I (%)	E_R $\sigma_a = 0.1$ MPa (J)	E_R/E_I (%)	ΔW (J)	$\Delta W/E_I$ (%)
SR1	1	12,10	12.8	N/A	N/A	1.2E−06	9.0E−06	1.1E−05	8.4E−05
SR2	1	15,10	19.0	N/A	N/A	1.8E−06	9.6E−06	4.3E−05	2.3E−04
SR3	1	20,10	7.5	5.1	72.6	8.9E−07	1.2E−05	4.3E−05	5.8E−04
SR4	1	30,10	12.6	9.9	78.8	1.0E−06	8.0E−06	7.8E−05	6.2E−04
IR1	0.25	20,10	26.5	4.8	18.2	1.9E−07	7.0E−07	9.0E−06	3.4E−05
IR2	0.5	20,10	14.2	13.4	94.0	3.3E−07	2.3E−06	1.6E−05	1.1E−04
IR3	2	20,10	16.5	15.1	91.3	1.2E−06	7.1E−06	5.7E−05	3.4E−04
IR4	4	20,10	14.9	10.9	73.1	2.7E−07	1.8E−06	1.3E−05	8.8E−05

[a] "SR" stands for stress ratio, and "IR" stands for injection rate.

For experiment SR4 ($\sigma_1 = 30$ MPa, $\sigma_3 = 10$ MPa) the total injection cycle for this experiment lasted for 257 s, where the pumping pressure reached a maximum value of 33 MPa (Figure 2). When the pumping pressure began to increase more rapidly at 215 s, the platens started to dilate in order to maintain a constant axial stress of 10 MPa. The main rupture began at 252.779 s, which corresponded with the starting time of the main pressure drop and lasted for 328.2 ms. The work done by the injection fluid on the axial platens is shown in Figure 2 as W_A. Just after peak pressure, there was a sudden drop in pressure, which was accompanied by a burst of AE activity and a further 0.135 mm of axial dilation. The AE activity was associated with the formation of a new fracture surface. The injection energy, which amounted to 12.63 J, was calculated using equation (3) and is presented in Figure 2. The work done by the fluid to open the newly created fracture (W_B) was calculated using equation (4) and amounted to 9.94 J. Fifty-two AE events were locatable and the majority of event locations occurred within a 1.5 s window coinciding with a large drop in fluid pressure (Figure 2). Event locations, projected on the $\sigma_1-\sigma_3$ plane, are presented in Figures 1b–1e. The induced disc-shaped fracture was oriented in the σ_1 plane, perpendicular to σ_3; however, it was not possible to track to propagation of the fracture due to the limited number of located events and the short duration of fracture formation. The fractured sample was scanned using high-intensity X-rays, and the reconstructed volume was analyzed to extract the induced fracture surface. The fracture surface is presented in Figures 1b–1e with 27.9 μm resolution and a calculated area of 7.741E−3 m². The fracture was initiated from the bottom of the borehole as determined from the μCT image and AE locations. Results from the other seven experiments followed the same general trends with the exception of experiments SR1 and SR2. These experiments were
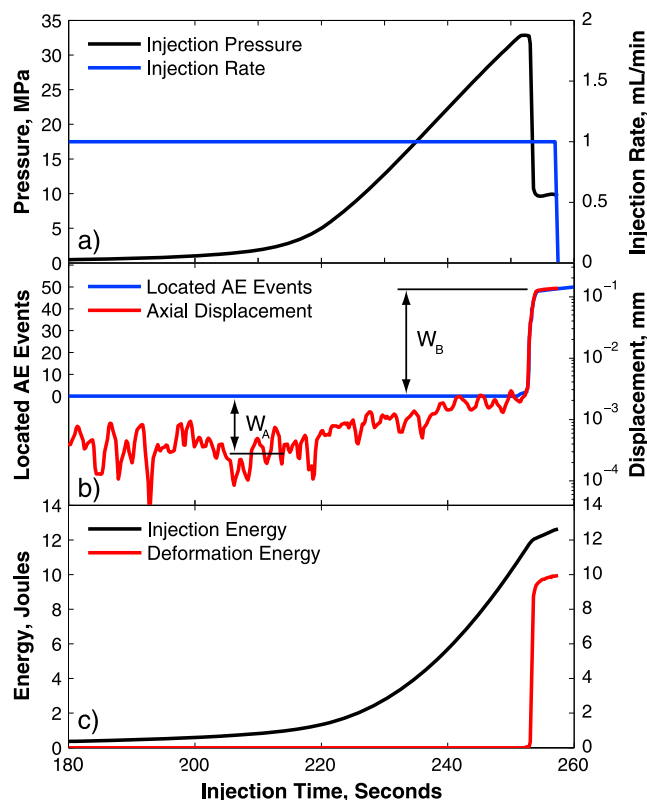
Figure 2. Experiment SR4 ($\sigma_1 = 30$ MPa, $\sigma_3 = 10$ MPa). (a) Injection pressure and injection rate. (b) Cumulative AE event locations and axial displacement. (c) Injection energy and deformation energy. All quantities plotted as a function of the injection time.

conducted at lower stress ratios which caused the formation of more complex fractures. For weak stress ratios, fractures were less constrained and small-scale heterogeneities become more influential; however, when the stress ratio was strong, small-scale heterogeneities lost their influence and fracture propagation was controlled by the surrounding stress field.

Seismic moments of located AE events were estimated using a spectral fitting method. From the seismic moment, we calculated the moment magnitude, which was found roughly in the range $-8.5 < M_w < -7$. The largest sources of uncertainty in estimating M_w were the sensor sensitivity, unknown attenuation properties, S wave windowing, and the single-component nature of the sensing instrument. The AE sensors were calibrated on an aluminum block, and therefore, we assumed that the sensitivity of the sensor, when attached to the rock specimen, was the same as when attached to the aluminum block (i.e., same coupling conditions). This same assumption was made by *Sellers et al.* [2003] and *Goodfellow and Young* [2014]; however, in the absence of a method for in situ calibration, we must consider this source of uncertainty. Another potential source of uncertainty is in the windowing of P and S waves. The presence of P wave, S wave, and reflected waves all occurring in such rapid succession, as a result of the small sample size, makes windowing the individual phases challenging and therefore a potential source of uncertainty.

We first estimated the total radiated seismic energy using the *Kanamori* [1978] relationship by converting seismic moment into energy and then summing all of the energies. Next we estimated the seismic energy using the apparent stress relationship of *Wyss and Brune* [1968], assuming constant σ_a values of 0.01 MPa and 0.1 MPa. The *Kanamori* [1978] method produced total seismic energies ranging from 1.93E−6 J to 1.87E−5 J, and using the apparent stress relationship of *Wyss and Brune* [1968] produced total seismic energies of 1.86E−8 to 1.82E−7 J ($\sigma_a = 0.01$ MPa) and 1.86E−7 to 1.82E−6 J ($\sigma_a = 0.1$ MPa) as shown in Table 1. The cumulative seismic energies were calculated using the largest AE events with sufficient signal to noise ratio; however, there were many more tiny events, as seen from the continuous waveform records, with poor signal to noise ratios, which could not be analyzed. Therefore, our calculations of cumulative seismic energy should be considered lower bound estimates. The b values were used to estimate the extent of missing small-magnitude AE data (see supporting information).

4. Discussion and Conclusion

For experiment SR4 ($\sigma_1 = 30$ MPa, $\sigma_3 = 10$ MPa) the total injection energy was calculated to be 12.63 J. The energy required to dilate a disc-shaped fracture with surface area 7.741E−3 m^2 by 0.135 mm was 9.94 J, and therefore, the deformation energy was 79% of the injection energy. For the other experiments, deformation energies ranged from 18% to 94% as seen in Table 1. The values for E_d in Table 1 are upper bound estimates (see supporting information for lower bounds). In the field, the method for estimating deformation energy is highly uncertain because fracture area is estimated using the distribution of microseismic event locations, fracture aperture is estimated from the proppant size, and a simple planar geometry is assumed although this is not always the case. In the field, the deformation energy is estimated to range from 15%–80% of the injection energy [*Maxwell et al.*, 2008; *Boroumand and Eaton*, 2012; *Warpinski et al.*, 2012], and therefore, for the majority of the experiments, what we calculated in the lab is at the high end, which is consistent with the expected lack of fluid leak-off and viscous dissipation. It is interesting to note that the experiment with the lowest injection rate (IR1, 0.25 mL/min) produced a deformation energy that was 18% of the injection energy, which was possibly a result of enhanced fluid leak-off. There are uncertainties in these calculations resulting from the averaging of LVDT measurements, the 5 Hz sampling rate, the fluid pressure measurement being made some distance from fracture, and the simplified model of a disc-shaped fracture instantaneously appearing and experiencing subsequent dilation (see supporting information). Given these uncertainties, we conclude that the deformation energy calculated in the laboratory is of the same order of magnitude as that calculated in the field and constitutes a significant term in the hydraulic fracture energy budget.

Figure 3a includes data from field-scale hydraulic fracture operations where induced fractures were on the order of hundreds of meters and moment magnitudes ranged from −3 to 1. The data are divided into induced seismicity (diamond symbols) and triggered seismicity (square symbols). Here we define induced seismicity as resulting from rupture that is driven by the human-related (induced) stress or pressure perturbation that would not occur without it and triggered seismicity as being triggered by some engineering process where the size of the event is controlled by the existing natural stress field and fault
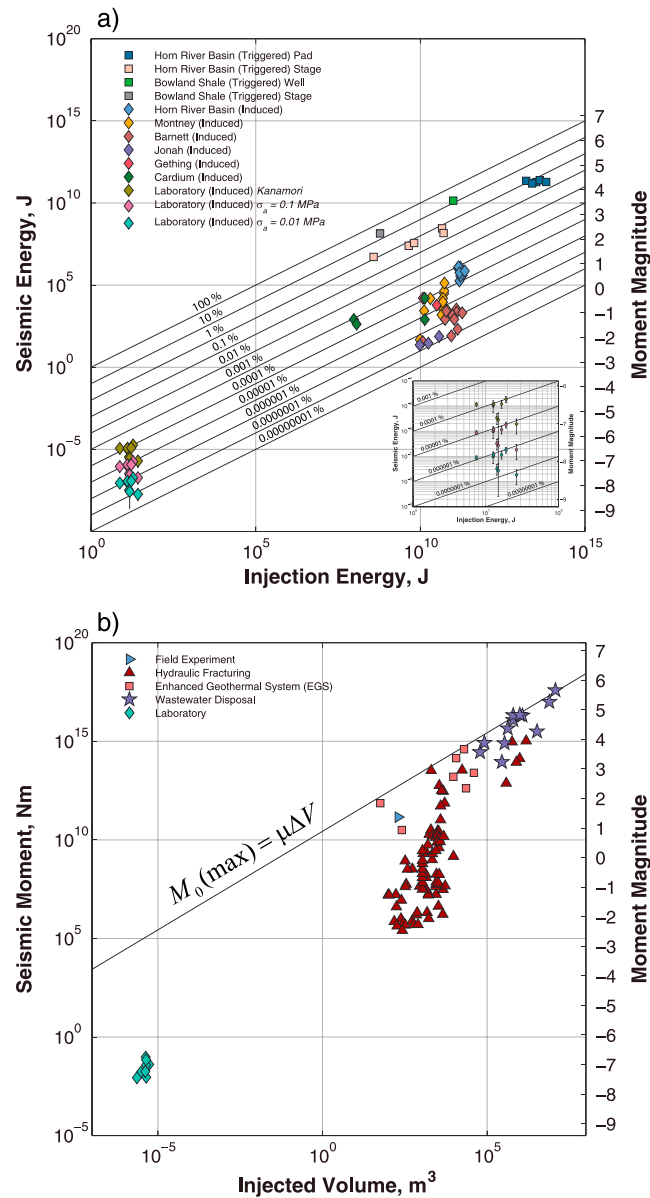
Figure 3. (a) Injection energy plotted against seismic energy. Reference lines correspond to the seismic injection efficiency in percentages. Square symbols refer to triggered seismicity, and diamond symbols refer to induced seismicity. M_w was calculated from seismic energy using *Kanamori* [1978]'s relationship. For more on classification (triggered/induced) of the field data, see *Maxwell et al.* [2008] and *Maxwell*, [2011, 2013]. (b) Seismic moment of the largest seismic event plotted against the total injected volume. The data presented in this plot were compiled by *McGarr* [2014] and *Maxwell* [2013] from numerous studies. These include field experiments, hydraulic fracturing, enhanced geothermal systems, and wastewater disposal. *McGarr*, 's [2014] injection model was calculated for $\mu = 27$ GPa.

structure [*Dahm et al.*, 2010]. Figure 3a shows seismic injection efficiencies ranging from 1E−7%–1E−3% for induced seismicity and 0.1%–5% for triggered seismicity [*Maxwell et al.*, 2008; *Maxwell*, 2013]. Figure 3a includes data from a range of geographic locations including Canada, the United States of America, and Britain.

The most conservative estimates of seismic energy (E_R) range from 1.86E−8 to 1.82E−7 J ($\sigma_a = 0.01$ MPa), which is equal to 7E−8 to 1.2E−6% of the injection energy. The supporting information includes correction factors for E_R calculated from b values, which account for missing small-magnitude data. The ratio of seismic energy to injection energy is referred to as the seismic injection efficiency [*Maxwell et al.*, 2008] and has been reported in the range 1E−7% to 1E−3% for unconventional hydraulic fracture plays [*Maxwell*, 2011; *Maxwell et al.*, 2008]. This range only considers induced seismicity; however, seismic injection efficiencies as high as 50% have been reported in the cases where increased seismic energy is attributed to tectonic stress release resulting from reactivation of existing faults. Figure 3a shows the injection energy plotted against the seismic energy, where reference lines correspond to seismic injection efficiency in percentages. A more robust measure of elastic energy release, as compared to E_R, is ΔW which was calculated from equation (2). Calculated values of ΔW for each experiment are presented in Table 1. Values for ΔW and $\Delta W/E_I$ range from 9.0E−6 J to 7.8E−5 J and 3.4E−5% to 6.2E−4%, respectively, which further supports the argument that elastic energy release is a minor component of the hydraulic fracture energy budget.

After studying microseismic data from a range of unconventional hydraulic fracture treatments, *Maxwell et al.* [2008] and *Warpinski et al.* [2012] concluded that the propagation of a hydraulic fracture is a largely aseismic process, and *Warpinski et al.* [2012] cautioned against inferring the stimulated reservoir volume from microseismic source analysis. In the laboratory, as in the field, we have shown that the amount of energy radiated as elastic waves is very small compared to the injection energy of the pump. Calculations of the volumetric increase caused by AE further support their conclusions. For experiment SR4 ($\sigma_1 = 30$ MPa, $\sigma_3 = 10$ MPa),

we recorded 52 AE events for which a b value of 2.49 ± 0.086 was calculated using the maximum likelihood method [*Aki*, 1965]. The b value was then used to correct for missing small-magnitude data resulting from poor signal to noise ratios. We also assume that each AE event has a corner frequency of 600 kHz, which implies a source radius of 2 mm [*Brune*, 1970, 1971], although *Cai et al.* [1998] clearly demonstrated that the source models of *Brune*, [1970, 1971] and *Madariaga* [1976] tend to overestimate the radius of small micro-seismic events (Westerly granite mean grain size is 0.75 mm). The slip distance can be calculated following $M_0 = \mu A d$, where μ is the shear modulus, A is the fracture area, and d is the slip distance. If we assume that all the slippage is opening, the total volumetric increase caused by AE is $4.9E-11$ m^3, which is $1.2E-3\%$ of the injected fluid volume.

McGarr [2014] proposed a model relating maximum seismic moment to volume change from fluid injection by the relationship $M_0(\max) = \mu \Delta V$, where μ is the shear modulus. Figure 3b presents M_0 of the largest recorded event during injection versus the total injected volume for multiple industrial and scientific injection projects. Enhanced geothermal system (EGS) and wastewater disposal events appear to generally follow *McGarr*,'s [2014] relationship which appears to define an upper limit on the magnitude of injection-induced seismicity. With the exception of a few cases, $M_0(\max)$ for a typical hydraulic fracture operation plots well below the modulus trend where in the vast majority of cases, a large-magnitude earthquake is not triggered [*Maxwell*, 2013]. The laboratory data also plot below the model prediction as would be expected given the intact nature of these experiments. This result suggests a similarity between laboratory hydraulic fractures in intact rock and hydraulic fractures in the field that are not associated with activation of existing fault systems.

In conclusion, we were able to successfully measure four components of the hydraulic fracture energy budget (E_I, ΔW, E_d, and E_R). Seismic injection efficiencies were $\ll 1\%$, which was consistent with a range of efficiencies for induced seismicity from field-scale hydraulic fracture operations. The majority of the injection energy was expended during the creation of a new fracture surface and subsequent fracture opening. The dominant term in the energy budget was the deformation energy which supports the conclusion of *Maxwell et al.* [2008] and *Warpinski et al.* [2012] that the principal deformation mechanism in a hydraulic fracture is largely aseismic.

References

Aki, M. (1965), Maximum likelihood estimate of b in the formula log $N = a - bM$ and its confidence limits, *Bull. Earthq. Res. Inst. Tokyo Univ.*, *43*, 237–239.

Aki, K., and P. Richards (1980), *Quantitative Seismology: Theory and Methods*, W. H. Freeman, New York.

Boore, D. M., and J. Boatwright (1984), Average body-wave radiation coefficients, *Bull. Seismol. Soc. Am.*, *74*, 1615–1621.

Boroumand, N., and D. W. Eaton (2012), Comparing energy calculations-hydraulic fracturing and microseismic monitoring, paper presented at CSEG GeoConvention, Canadian Society of Exploration Geophysicists, Calgary, Canada, 14–18 May.

Brune, J. N. (1970), Tectonic stress and spectra of seismic shear waves from earthquakes, *J. Geophys. Res.*, *75*, 4997–5009.

Brune, J. N. (1971), Correction, *J. Geophys. Res.*, *76*, 5002.

Cai, M., P. Kaiser, and C. Martin (1998), A tensile model for the interpretation of microseismic events near underground openings, *Pure Appl. Geophys.*, *153*, 67–92.

Collins, D. S., and R. P. Young (2000), Lithological controls on seismicity in granitic rocks, *Bull. Seismol. Soc. Am.*, *90*, 709–723.

Dahm, T., et al. (2010), How to discriminate induced, triggered and natural seismicity, *paper presented at the Workshop Induced seismicity: November 15–17, 2010, Luxembourg, Grand-Duchy of Luxembourg*, (Cahiers du Centre Europen de Godynamique et de Sismologie, 30), Centre Europen de Godynamique et de Sismologie, 69–76.

Goodfellow, S. D., and R. P. Young (2014), A laboratory acoustic emission experiment under in situ conditions, *Geophys. Res. Lett.*, *41*, 3422–3430, doi:10.1002/2014GL059965.

Ide, S., and G. Beroza (2001), Does apparent stress vary with earthquake size?, *Geophys. Res. Lett.*, *28*, 3349–3352.

Kanamori, H. (1978), Quantification of earthquakes, *Nature*, *271*, 411–414.

Kanamori, H., and D. L. Anderson (1975), Theoretical basis of some empirical relations in seismology, *Bull. Seismol. Soc. Am.*, *65*, 1073–1095.

Kanamori, H., and E. E. Brodsky (2004), The physics of earthquakes, *Rep. Prog. Phys.*, *67*, 1429–1496.

Kwiatek, G., K. Plenkers, and G. Dresen (2011), Source parameters of picoseismicity recorded at Mponeng deep gold mine, South Africa: Implications for scaling relations, *Bull. Seismol. Soc. Am.*, *101*, 2592–2608.

Lockner, D. A., J. D. Byerlee, V. Kuksenko, and A. Sidorin (1991), Quasi-static fault growth and shear fracture energy in granite, *Nature*, *350*, 39–42.

Madariaga, R. (1976), Dynamics of an expanding circular fault, *Bull. Seismol. Soc. Am.*, *66*, 639–666.

Maxwell, S. C., J. Schemeta, E. Campbell, and D. Quirk (2008), Microseismic deformation rate monitoring, *paper presented at SPE Annual Technical Conference and Exhibition*, SPE–116596-MS, Denver, Colo., 21–24 Sept.

Maxwell, S. C. (2011), What does microseismic tell us about hydraulic fracture deformation, *CSEG Recorder*, *36*.

Maxwell, S. C. (2013), Unintentional seismicity induced by hydraulic fracturing, *CSEG Recorder*, *38*.

McGarr, A. (2014), Maximum magnitude earthquakes induced by fluid injection, *J. Geophys. Res.*, *119*, 1008–1019.

McLaskey, G. C., and S. D. Glaser (2012), Acoustic emission sensor calibration for absolute source measurements, *J. Nondest. Eval.*, *31*, 157–168.

Sellers, E. J., M. O. Kataka, and L. M. Linzer (2003), Source parameters of acoustic emission events and scaling with mining-induced seismicity, *J. Geophys. Res.*, *108*(B9), 2418, doi:10.1029/2001JB000670.

Thompson, B. D., R. P. Young, and D. A. Lockner (2006), Fracture in Westerly granite under AE feedback and constant strain rate loading: Nucleation, quasi-static propagation, and the transition to unstable fracture propagation, *Pure Appl. Geophys.*, *163*, 995–1019.

Thompson, B. D., R. P. Young, and D. A. Lockner (2009), Premonitory acoustic emissions and stick-slip in natural and smooth-faulted Westerly granite, *J. Geophys. Res.*, *114*, B02205, doi:10.1029/2008JB005753.

Warpinski, N. R., J. Du, and U. Zimmer (2012), Measurements of hydraulic-fracture-induced seismicity in gas shales, *paper presented at SPE Hydraulic Fracturing Technology Conference*, Soc. Petrol. Eng., Texas, 6–8, Feb.

Wyss, M., and J. N. Brune (1968), Seismic moment, stress and source dimensions for earthquakes in the California-Nevada region, *J. Geophys. Res.*, *73*, 4681–4694.